Applied Thermal Engineering 248 (2024) 123192

Contents lists available at ScienceDirect

Applied Thermal Engineering

journal homepage: www.elsevier.com/locate/apthermeng

Research Paper

Thermodynamic and optimization analysis of a fuel cell-based combined cooling, heating, and power system integrated with LNG-fueled chemical looping hydrogen generation

Yadong Du [a,b], Zhiyi Yu [a], Ce Yang [a,*], Haimei Wang [a,b], Buchen Wu [b,c,**]

[a] School of Mechanical Engineering, Beijing Institute of Technology, Beijing 100081, China
[b] Department of Mechanical Engineering, National University of Singapore, 9 Engineering Drive 1, Singapore 117576, Singapore
[c] Department of Mechanical and Aerospace Engineering, The Hong Kong University of Science and Technology, Clear Water Bay, Kowloon, Hong Kong

ARTICLE INFO

Keywords:
Combined cooling, heating, and power system
Liquid natural gas regasification process
Chemical looping hydrogen generation
Solid oxide fuel cell
CO_2 capture

ABSTRACT

Chemical looping combustion technology is essential to achieve efficient decarbonized electricity generation for fossil-fueled power plants. However, the existing chemical looping hydrogen generation (CLHG)-driven cogeneration systems have complex refrigeration units and energy-consuming carbon capture. This study proposes a novel solid oxide fuel cell (SOFC)-based combined cooling, heating, and power (CCHP) system, which is integrated with the CLHG and fueled by a liquid natural gas (LNG) regasification process. The system is designed to enhance the overall performance by directly recovering LNG cold energy for cooling and liquefying the resulting CO_2. The energy and exergy performance of the system under the baseline design case are evaluated. Subsequently, we discuss the impact of key design parameters on system performance and weigh between cooling/heating power and net power generation for the system dominated by the combined heat and power (CHP)/combined cooling and power (CCP) mode. Our findings reveal that the proposed system exhibits an electrical efficiency of 66.92 % and an exergy efficiency of 53.94 % under the baseline design case. The exergy loss ratio for condenser1 is identified as the highest among all components, accounting for 29.50 %. The constituent unit with the largest exergy loss contribution is the LNG regasification unit, followed by the SOFC unit, CLHG unit, transcritical CO_2 cycle unit, and heating unit. More hydrogen needs to be replenished when fuel flow in the CLHG and fuel utilization in the SOFC are used to improve system performance. The optimal electrical and exergy efficiencies of the system predominantly designed in CCP mode surpass those in CHP mode by 4.27 % and 0.57 %, respectively. The results can guide potential applications of CLHG-based cogeneration systems.

1. Introduction

The escalation in carbon emissions, concomitant with an enhancement in people's living standards, has triggered a series of challenges, notably encompassing climate change and environmental pollution. To avoid the exacerbation of these issues, a total of 77 nations have committed to attain carbon neutrality by the year 2050 [1]. Despite global efforts to develop renewable energy sources, such as solar and wind power, it remains noteworthy that fossil fuel-based electricity production continues to account for 63 % share of global electricity generation [2,3]. Consequently, carbon capture and storage (CCS) technologies become indispensable for achieving decarbonized electricity generation. Among the currently prevailing carbon capture techniques, pre- and post-combustion capture approaches pose significant limitations on energy efficiency, resulting in efficiency reductions of approximately 7–10 percentage points and 10–15 percentage points, respectively [4,5]. Moreover, the utilization of oxy-fuel combustion presents an additional challenge, characterized by diminished power generation efficiency due to the considerable power consumption entailed by the air separation unit [6]. Fortunately, the innovative concept of chemical looping combustion (CLC), originally advanced by Richter and Knoche [7], has emerged as a promising and effective way to compensate for the inherent limitations of the existing carbon capture methodologies, thereby facilitating the realization of highly efficient decarbonized power generation.

The CLC system is primarily composed of reactors serving distinct functions and an oxygen carrier endowed with a support phase [8]. The

* Corresponding author at: The Turbomachinery Institute, School of Mechanical Engineering, Beijing Institute of Technology, Beijing 100081, China.
** Corresponding author at: Department of Mechanical Engineering, National University of Singapore, 9 Engineering Drive 1, Singapore 117576, Singapore.
E-mail addresses: YANGCE@BIT.EDU.CN (C. Yang), BUCHENWU@U.NUS.EDU (B. Wu).

https://doi.org/10.1016/j.applthermaleng.2024.123192
Received 8 January 2024; Received in revised form 23 March 2024; Accepted 15 April 2024
Available online 16 April 2024

Nomenclature

A	area, m^2
$\dot{E}$	exergy rate, kW
F	Faraday constant, C/mol
h	enthalpy, kJ/kg
I	exergy loss, kW
i	current density, A/m^2
$\dot{m}$	mass flow rate, kg/s
$\dot{n}$	molar flow rate, mol/s
p	pressure, MPa
Q	heat transfer, kW
s	entropy, kJ/(kg × K)
T	temperature, ℃
Uti	fuel utilization
V	voltage, V
W	power, MW

Greek letters

ε	regenerator effectiveness
η	efficiency
θ	exergy loss ratio

Subscripts

ch	chemical
el	electrical
ex	exergy
net	net power generation
ph	physical

Abbreviations

AR	air reactor
CCHP	combined cooling, heating, and power
CCP	combined cooling and power
CCS	carbon capture and storage
CLC	chemical looping combustion
CHP	combined heat and power
FR	fuel reactor
GT	gas turbine
LNG	liquid natural gas
SOFC	solid oxide fuel cell
SR	steam reactor
TRCC	transcritical CO_2 cycle

iron-, chromium-, and tungsten-based CLCs have demonstrated the capability to effectuate carbon separation and hydrogen production [9]. Particularly, iron oxide is a typical choice for chemical looping hydrogen generation (CLHG) due to its multiple advantages, including high fuel conversion efficiency, a high melting point, catalytic activity, resilience to carbon deposition, low cost, and environmental compatibility [10]. The iron-based CLHG system is structured by a fuel reactor (FR), a steam reactor (SR), an air reactor (AR), and oxygen carriers exhibiting varying iron valences as they circulate among these reactors. De Vos et al. [11] have experimentally demonstrated the successful mitigation of oxygen carrier deactivation after several cycles by replacing the Al_2O_3-support with $MgAl_2O_4$. After conducting experiments on a $MgAl_2O_4$-supported iron-based CLHG system, Ryden and Arjmand [12] affirmed that the amount of hydrogen generated within the steam reactor aligned closely with the quantity of fuel oxidized in the fuel reactor. Kong et al. [13] unveiled that the exergy efficiency of the iron-based CLHG system outperformed that of the conventional steam-methane reforming (SMR) process by 4.3 percentage points. Yan et al. [14] proposed an integrated hydrogen cogeneration system based on slurry-feed coal gasification and CLHG. The results underscored that the hydrogen production rate, CO_2 capture rate, energy efficiency, and thermal efficiency of the system were 1040.11 kg/h, 94.56 %, 46.21 %, and 47.22 %, respectively. He et al. [15] proposed a novel CH_4-fueled CLHG configuration designed for the simultaneous synthesis of liquid fuel and power generation. They found that the fuel energy saving and CO_2 emission rates of the proposed system were projected to be 12.19 % and 98.46 %, respectively, relative to separate production systems. Ghannadi and Dincer [16] propounded a CLHG combined solar-powered cogeneration system. The findings were that the system had an energy efficiency of 27 %, an exergy efficiency of 25 %, a hydrogen production rate of 10.5 kg/s, and a CO_2 capture rate of 1,120 kg/s.

The generated hydrogen can be stored or used directly [17–19]. Utilizing hydrogen generated by CLHG, solid oxide fuel cells (SOFC) can convert the chemical energy of the fuel into electricity efficiently without the constraints of the Carnot cycle [20]. SOFCs exhibit the capacity for operation at elevated pressures, with typical operating temperatures ranging from 700 °C to 1000 °C. Consequently, they can be combined with a gas turbine (GT) to constitute an integrated power generation system. Another advantage is the harnessing of high-grade waste heat of the expanded gas, which can produce electricity by driving thermal systems. The subsequent low-grade waste heat can be supplied to the heating and cooling units. Ni et al. [21] and Zhang et al. [22] introduced a supercritical CO_2 Brayton cycle (SCBC) combined organic Rankine cycle as the downstream system of SOFC, achieving the efficient utilization of energy cascades. Researchers such as Liu et al. [23], Zeng et al. [24], and Azhar et al. [25] have explored diverse configurations of SOFC-based combined cooling, heating, and power (CCHP) systems, achieving 62.27 %, 59.08 %, and 63.29 % of exergy efficiency, respectively. Furthermore, compared to SOFCs fueled by natural gas, H_2-fuelled SOFCs do not require a carbon capture process due to the absence of CO_2 generation. Thus, scholars have delved into the exploration of CCHP systems propelled by an integrated synergy of CLHG and SOFCs. Zhao et al. [26] employed a transcritical CO_2 cycle (TRCC) and chilled water for the recovery of waste heat from a CLHG/SOFC system. The results showed that the energy, power generation, and exergy efficiencies of the system exceeded 80 %, 65 %, and 60 %, respectively. Wang et al. [27] proposed a diesel-fueled CLHG/SOFC cogeneration system with CO_2 recovery. The power generation efficiency, exergy efficiency, and fuel energy saving ratio of the proposed system were 64 %, 60 %, and 60 %, respectively. They also investigated the thermodynamic performance of a new SOFC-CCHP system using CLHG-reformed diesel for hydrogen production [28]. Their findings were that the system's power generation efficiency was 54.1 %, while the exergy efficiency and fuel energy saving ratio were both about 53 %. Hao et al. [10] introduced a CLHG/SOFC-based zero-energy penalty carbon capture and utilization system for electricity and methanol cogeneration. The proposed system achieved an optimal energy efficiency of 70.94 %, concomitant with a remarkable CO_2 capture rate of 98.54 %. Ma et al. [29] analyzed the thermodynamic performance of a SOFC-based CCHP system incorporating solar and CLHG. Their results manifested energy and exergy efficiencies of 78.02 % and 45.92 % in cooling mode and 72.94 % and 46.59 % in heating mode, highlighting the potential of these integrated systems in diverse operational modes.

For the CLHG/SOFC-driven CCHP systems, the cooling function is fulfilled through an adsorption refrigeration cycle subsystem [28,29]. However, when an NG-fueled CLHG system includes a liquid natural gas (LNG) regasification process, the additional refrigeration cycle becomes redundant, leaving all the low-grade waste heat dedicated to the heating unit. Presently, some researchers have developed CCHP systems based on NG-fueled gas turbines or SOFCs by recovering the inherent cooling

energy of LNG. Cha et al. [30] implemented a GT-CO_2 combined cycle, integrating inlet cooling and heat recovery using LNG cold energy. By comparison, they discerned that the incorporation of inlet cooling and heat recovery increased the power and efficiency of the combined cycle by 14.9 % and 2.1 %, respectively. Su et al. [31] proposed a CCP system integrating a GT, an SCBC, and a TRCC by recovering the cold energy of LNG. The thermal and exergy efficiencies of the combined system were 52.94 % and 30.27 %, respectively. Li and Wang [32] investigated the performance of a cascade TRCC system, which is heated and cooled by GT waste heat and LNG cold energy, respectively. The optimization results showed the system with an exergy efficiency of 49.24 % and a net power of 15.53 MW. Liang et al. [33] proposed a near-zero emission polygeneration system consisting of SOFC, LNG cold energy recovery, ORC, and TRCC. The system achieved thermal, net electrical, and exergy efficiencies of 90.99 %, 55.01 %, and 53.07 %, respectively, at rated operating conditions. After integrating SOFC-GT, CO_2 cycles, ORC, and LNG regasification processes into a CCHP system, Liu et al. [34] found that the energy, net power generation, and exergy efficiencies of the system were 79.48 %, 79.81 %, and 62.29 %, respectively.

The above literature review underscores the pivotal role of the adsorption refrigeration sub-cycle in providing cold energy within the NG-fueled CLHG/SOFC-driven CCHP system. Nevertheless, the adsorption refrigeration unit can be replaced with an LNG regasification process to reduce the system's complexity. The cold energy recovery of LNG has been seen in various cases of GT-driven and SOFC-driven CCHP systems. Consequently, it is imperative to propose a CLHG/SOFC-driven CCHP system featuring LNG cold energy recovery and to confirm its theoretical feasibility thermodynamically, but this is still a research gap. When a high-efficiency TRCC is employed to convert the high-grade waste heat of the SOFC-GT into electricity, the saturation temperature of the liquid CO_2 can be effectively lowered by recovering the LNG cold energy via a sub-zero temperature heat sink to amplify the output power of the unit at a constant maximum pressure. Furthermore, due to the varying cooling and heating power demands in different regions, the maximum design power of the system needs to be assessed when combined heat and power (CHP) and combined cooling and power (CCP) modes are predominant, respectively. Therefore, a CLHG/SOFC-driven cogeneration system fueled by LNG regasification enables efficient generation of cooling, heating, and electricity with near-zero carbon emissions. The main contributions of this study are as follows:

(1) An LNG-fueled CLHG/SOFC-driven CCHP system is proposed, which directly utilizes LNG cold energy to cool CO_2 to a liquid state for storage.

(2) The effects of key parameters on system output power, thermal efficiency, and exergy efficiency are comprehensively discussed.

(3) The design power of the system was optimized with CHP or CCP as the dominant mode, respectively.

The remainder of the article is organized as follows: Section 2 describes the operating principle of the system. System modeling and validation are presented in Section 3. The results and discussion on the system's performance advantages, exergy distribution under the baseline design case, and parameter optimization analysis are shown in Section 4. The key findings are summarized in Section 5.

2. System description

The proposed CCHP system is shown in Fig. 1, which consists of an LNG regasification unit, a CLHG unit, a SOFC-GT unit, a TRCC unit, and a hot water supply unit. The operation principle of each unit is as follows:

In the LNG regasification unit, the liquid fuel pressurized by the fuel pump (FP) is preheated to a gaseous state in two condensers. The low-temperature NG then enters the cooler to cool the tap water for cold energy output. Subsequently, a portion of the NG is channeled into the CLHG unit, while the remaining portion is distributed for user consumption.

In the iron-based CLHG unit, the outlet of each reactor is connected to a gas–solid separator (GSS). The gaseous fuel preheated by the heat

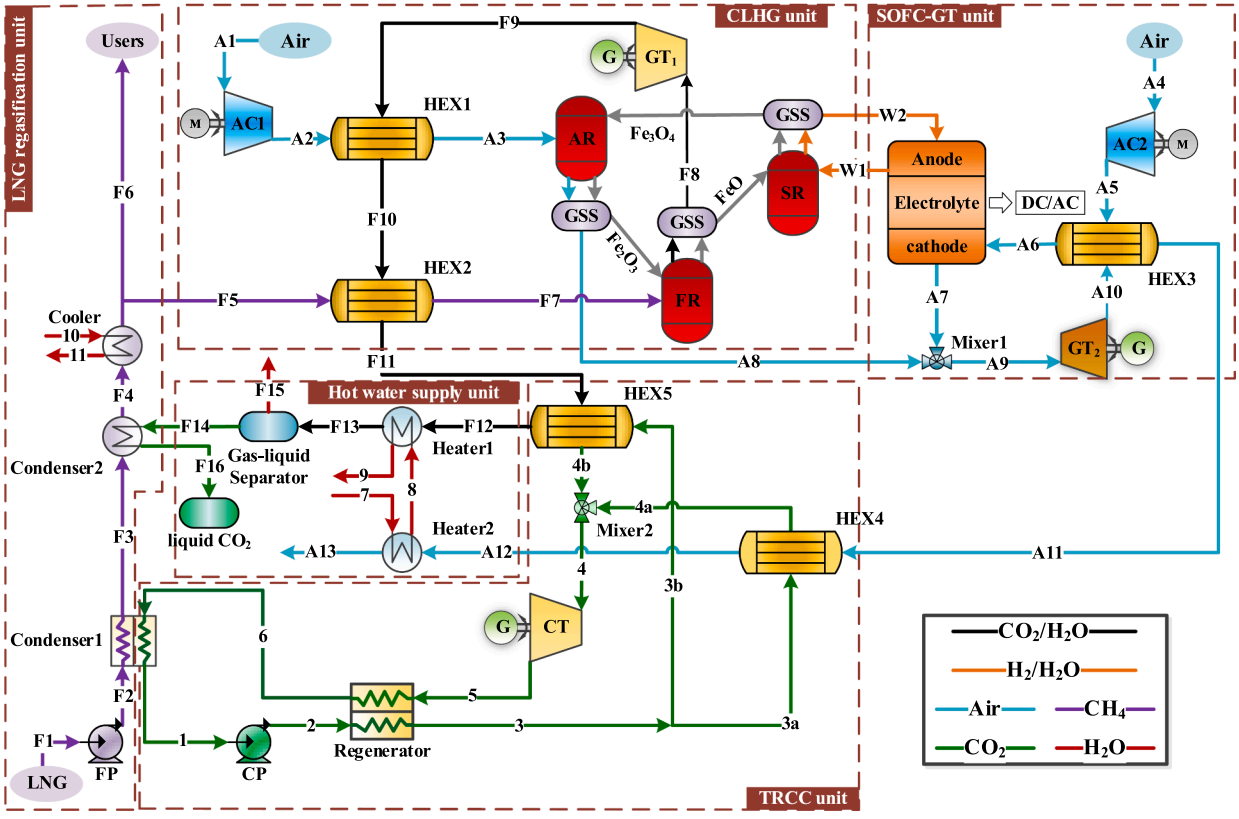

Fig. 1. The CLHG/SOFC-driven CCHP system with LNG cold energy recovery.

exchanger (HEX2) enters the FR and reacts with Fe_2O_3 to generate FeO, water, and CO_2. This endothermic reaction relies predominantly on heat sourced from the $MgAl_2O_4$-support. The resulting water-CO_2 mixture expands in the GT1 and then successively heats the air and NG before entering the downstream units. The FeO enters the SR, where it undergoes an exothermic reaction with water vapor emanating from the SOFC anode, producing Fe_3O_4 and H_2. To ensure the complete conversion of FeO to Fe_3O_4, an excess of water vapor is maintained, resulting in a gas mixture predominantly comprising H_2 directed towards the SOFC anode. The Fe_3O_4 then proceeds to the AR, where it is oxidized by the compressed and preheated excess air to Fe_2O_3. This oxidation process elevates the temperature of the products due to the heat released during the reaction. Finally, the regenerated Fe_2O_3 is cycled back to the FR for reduction again, while the nitrogen-rich air is channeled into the GT2 for expansion.

In the SOFC-GT unit, H_2 is introduced into the anode as fuel, while air is supplied to the cathode, facilitating the operation of the SOFC for electricity generation. The closed loop that connects the anode of the SOFC with the FR of the iron-based CLHG avoids direct fuel combustion by eliminating the afterburner. The high-temperature nitrogen-rich air emanating from both the SOFC cathode and the AR is merged and subsequently directed into the GT2. The expanded nitrogen-rich air progresses to the downstream unit after preheating the air compressed by the air compressor (AC2). Due to the incomplete conversion of H_2, the amount of water vapor at the anode outlet is not sufficient to meet the demand of the SR. Therefore, the supplementation of H_2 is critical to maintaining the stable operation of the system, as highlighted in Ref. [26].

In the TRCC unit, the saturated liquid CO_2 exiting the condenser1 is pressurized to a subcooled state by the CO_2 pump (CP). After absorbing heat in the regenerator, the high-pressure CO_2 is heated to a supercritical state by the parallel HEX4 and HEX5. Then, the supercritical CO_2 expands to a superheated state in the CO_2 turbine (CT). The superheated CO_2 undergoes cooling in the regenerator before entering the condenser1, where it is returned to its saturated liquid state.

The hot water supply unit incorporates a CO_2 capture process. The heating of tap water is executed in two stages, initially in heater2 and then in heater1. Concurrently, the water vapor present in the mixture is condensed to a liquid state in heater1. The liquid water is then separated from the gaseous components in a gas–liquid separator (GLS), facilitating CO_2 capture. The separated gaseous CO_2 is cooled to a liquid state in the condenser2 for storage.

3. System modeling and analysis methods

3.1. Basic assumptions

This study uses MATLAB [35] and ASPEN PLUS [36] to simulate the CCHP system. The simulation process involves importing the results of the CLHG unit, obtained from ASPEN PLUS, into MATLAB. This allows for the simulation of other units within the system and facilitates the calculation of various performance metrics. All reactors of the CLHG are of the RGibbs type with an operating pressure equal to the inlet pressure of the reactants. The physical properties are obtained by calling the Peng-Robinson function in ASPEN PLUS and the NIST REFPROP [37] in MATLAB. The simulation adheres to the principles of mass and energy conservation, as well as the principle of chemical equilibrium determined by minimizing Gibbs free energy. The baseline design parameters of the system are outlined in Table 1. The isentropic efficiencies of the pump, compressor, gas turbine, and CO_2 turbine are 80 %, 82 %, 75 %, and 80 %, respectively [26]. During the simulation process, several assumptions are made to streamline the analysis:

(1) The system operates at a steady state, with no leakage of the working medium.

(2) The composition of LNG is CH_4, and the composition of air is 21 % O_2 and 79 % N_2.

Table 1
Baseline design parameters for the CCHP system.

Item	Values
LNG regasification unit	
Pump inlet temperature, °C [31]	−162
Pump outlet pressure, bar [26]	5
Cooler inlet temperature, °C	−80
Cooler outlet temperature, °C [31]	5
Water temperature after cooling, °C [31]	5
CLHG unit	
Fuel flow into the FR, kmol/h [38]	1
$MgAl_2O_4$ flow, kmol/h [38]	6
Fe_2O_3 flow, kmol/h [38]	4
FR intake temperature, °C [38]	450
AR intake temperature, °C [38]	470
CLHG operating pressure, bar [26]	5
CLHG excess air and water coefficient [26]	1.1
SOFC-GT unit	
Air temperature into SOFC, °C [27]	500
SOFC active surface, m^2 [39]	96.1
SOFC operating temperature, °C [39]	910
SOFC operating pressure, bar [26]	5
SOFC heat loss, % [39]	2
Fuel utilization factor, % [39]	85
DC to AC inverter efficiency, % [26]	95
TRCC and heating units	
CP inlet pressure, bar [31]	15.9
CP outlet pressure, bar [31]	133
HEXs outlet temperature difference, °C [31]	25
Outlet temperature of HEXs, °C	150
Regenerator effectiveness, % [31]	70
Water temperature after heating, °C [29]	65
GLS operating temperature, °C [26]	45
Nitrogen-rich air exhaust temperature, °C	100

(3) All components are adiabatic, and their pressure drop is neglected.

(4) There are no side reactions within each reactor, and the exit temperatures of the gaseous and solid products are equal.

(5) The gas–solid separation of the separators connected to each reactor is complete.

(6) The voltage of the SOFC is maintained stable, and the exhaust gas temperatures at both the cathode and anode equal the operating temperature of the SOFC.

(7) The ambient temperature and pressure are 25 °C and 101.325 kPa, respectively.

3.2. Chemical looping hydrogen generation model

The iron-based CLHG unit utilizes iron-based oxygen carriers circulating between reactors to prevent direct contact between air and fuel by dividing the reaction process into three steps. The specific reactions are as follows:

$$\mathrm{FR}: 4Fe_2O_3 + CH_4 \rightarrow 8FeO + CO_2 + 2H_2O \ \Delta H = +356.6\mathrm{kJ/kmol} \quad (1)$$

$$\mathrm{SR}: 8FeO + \frac{8}{3}H_2O \rightarrow \frac{8}{3}Fe_3O_4 + \frac{8}{3}H_2 \ \Delta H = -199.3\mathrm{kJ/kmol} \quad (2)$$

$$\mathrm{AR}: \frac{8}{3}Fe_3O_4 + \frac{2}{3}O_2 \rightarrow 4Fe_2O_3 \ \Delta H = -314.6\mathrm{kJ/kmol} \quad (3)$$

Therefore, the overall reaction that occurs in the CLHG is exothermic as follows:

$$CH_4 + \frac{2}{3}H_2O + \frac{2}{3}O_2 \rightarrow CO_2 + \frac{8}{3}H_2 \ \Delta H = -157.4\mathrm{kJ/kmol} \quad (4)$$

3.3. Solid oxide fuel cell model

The three important parameters during performing SOFC simulation are battery current, voltage, and efficiency. The current is shown as Eqs.

(5) and (6).

$$I = zn_eF \tag{5}$$

$$i = I/A_{SOFC} \tag{6}$$

where I represents the current, A. z is the molar flow rate of hydrogen involved in the reaction, mol/s. n_e is the number of electrons per mole of fuel. F is the Faraday constant, 96,485 C/mol. i is the current density, A/m^2. A_{SOFC} is the active surface area of the SOFC, m^2.

The voltage includes open circuit voltage and polarization voltage. The procedure for calculating the voltage of a H_2-fueled SOFC is as follows.

$$V_0 = 1.253 - 2.4516 \times 10^{-4}T \tag{7}$$

$$V = V_0 + \frac{RT}{2F}\ln\left(\frac{p_{H_2}p_{O_2}^{0.5}}{p_{H_2O}}\right) \tag{8}$$

$$V_{SOFC} = V - V_{ohm} - V_{act} - V_{con} \tag{9}$$

where V_0 is the standard electric potential, V. T is the operating temperature, K. V is the theoretical open circuit voltage, V. R is the molar gas constant, 8.3145 J/(mol·K). p_{H2} and p_{H2O} are the partial pressures of hydrogen and water vapor at the anode outlet, respectively, bar. p_{O2} is the partial pressure of oxygen at the cathode outlet, bar. Vohm is the ohmic polarization voltage, V. Vact is the activation polarization voltage, V. Vcon is the concentration polarization voltage, V.

The ohmic polarization voltage is expressed as Eqs. (10)-(12).

$$P_k = a_k\exp\left(\frac{b_k}{T}\right) \tag{10}$$

$$r_k = \frac{P_k\delta_k}{A} \tag{11}$$

$$V_{\text{ohm}} = I\sum\delta_k \tag{12}$$

where r_k is the ohmic resistance of the cell, Ω. P_k is the resistivity of the response component, Ω·m. δ_k is the thickness, mm. The values of the relevant parameters for calculating Eqs. (10)-(12) are listed in Table 2.

The decrease in voltage caused by the slow reaction at the electrode–electrolyte interface is called the activated polarization voltage, which is calculated by Eqs. (13)-(17).

$$i_0^{an} = Y_{an}\left(\frac{p_{H_2}}{p_{an}^0}\right)\left(\frac{p_{H_2O}}{p_{an}^0}\right)\exp\left(-\frac{E_{act,an}}{RT}\right) \tag{13}$$

$$i_0^{ca} = Y_{ca}\left(\frac{p_{O_2}}{p_{ca}^0}\right)^{0.25}\exp\left(-\frac{E_{act,ca}}{RT}\right) \tag{14}$$

$$V_{act}^{an} = \frac{RT}{F}\ln\frac{i}{2i_0^{an}} + \left(\left(\frac{i}{2i_o^{an}}\right)^2 + 1^{0.5}\right) \tag{15}$$

$$V_{act}^{ca} = \frac{RT}{F}\ln\frac{i}{2i_0^{ca}} + \left(\left(\frac{i}{2i_0^{ca}}\right)^2 + 1^{0.5}\right) \tag{16}$$

$$V_{act} = V_{act}^{an} + V_{act}^{ca} \tag{17}$$

Table 2
Ohmic polarization parameters [26,28].

Item	a (Ω·m)	b (K)	δ (mm)
Cathode	0.0000811	600	2.20
Anode	0.0000298	−1392	0.10
Electrolyte	0.0000294	10,350	0.04
Connector	0.0012	4690	0.085

where Y is the diffusion coefficient, A/m^2. E is the activation energy, J/mol. p^0 is the reference pressure at the electrode surface, 1 bar. i_0 is the exchange current density, A/m^2. The values of the relevant parameters for calculating Eqs. (13)-(17) are listed in Table 3.

The concentration polarization voltage is caused by the migration of the electrode and interface materials. Usually, the concentration polarization can be neglected when the SOFC's operating temperature is high and diffusion proceeds efficiently [40].

The output power and generation efficiency of the SOFC stack are expressed as Eqs. (18) and (19), respectively.

$$W_{SOFC} = I \times V_{SOFC} \times \eta_{DC-AC} \tag{18}$$

$$\eta_{SOFC} = \frac{W_{SOFC}}{(\dot{m} \times LHV)_{H_2}} \tag{19}$$

where $\dot{m}$ is the mass flow rate of the input H_2. LHV is the low heating value of H_2, 120 MJ/kg.

3.4. Calculation model of other units

The method of modeling compression components using isentropic efficiency is shown as Eqs. (20) and (21).

$$\eta = \frac{h_{out,s} - h_{in}}{h_{out} - h_{in}} \tag{20}$$

$$W = \dot{m} \times (h_{out} - h_{in}) \tag{21}$$

where h_{in} and h_{out} are the inlet enthalpy and outlet enthalpy of the component, respectively. The subscript $_s$ represents the isentropic condition.

The method of modeling turbine using isentropic efficiency is shown as Eqs. (22) and (23).

$$\eta = \frac{h_{in} - h_{out}}{h_{in} - h_{out,s}} \tag{22}$$

$$W_{\text{Turbine}} = \dot{m} \times (h_{out} - h_{in}) \tag{23}$$

The heat transfer in the heat exchanger is expressed as Eq. (24). The regenerator in the TRCC unit is modelled using the effectiveness as Eq. (25).

$$Q = \dot{m}_c \times (h_{out} - h_{in}) = \dot{m}_h \times (h_{in} - h_{out}) \tag{24}$$

$$\varepsilon = \frac{T_{h,in} - T_{h,out}}{T_{h,in} - T_{c,in}} \tag{25}$$

where Q represents the heat transfer. ε is the regenerator effectiveness. The subscripts $_{h,\ c}$ are the hot and cold fluids, respectively.

3.5. Exergy analysis

To break through the inability of the first law of thermodynamics to characterize the quality difference of energy, exergy analysis based on the second law of thermodynamics has emerged. Exergy analysis is an important tool for evaluating the energy utilization of a thermal system and reflecting the weaknesses of the system by revealing the exergy flow distribution of the components. The exergy calculation for each node in the system is shown as Eqs. (26)-(28).

Table 3
Activation polarization parameters [26].

Item	Value
$E_{act,an}$ (J/mol)	1.10×10^5
$E_{act,an}$ (J/mol)	1.55×10^5
$Y_{ca,an}$ (A/m^2)	7.00×10^9

$$\dot{E} = \dot{E}_{ch} + \dot{E}_{ph} \tag{26}$$

$$\dot{E}_{ph} = \dot{m} \times [(h - h_0) - T_0(s - s_0)] \tag{27}$$

$$\dot{E}_{ch} = \dot{n} \times \left[\sum x_i e_i + RT_0 \sum x_i \ln x_i \right] \tag{28}$$

where $\dot{E}_{ch}$ and $\dot{E}_{ph}$ denote chemical exergy and physical exergy, respectively. s denotes entropy. $\dot{n}$ is the molar flow rate. x_i and e_i are the molar fraction of the i^{th} component in the flow stream and the standard chemical exergy, respectively. The standard chemical exergy for CH_4 and H_2 are 836.51 kJ/kmol and 238.49 kJ/kmol, respectively [41].

The exergy balance equation and exergy loss ratio for the k^{th} component are expressed as Eqs. (29) and (30), respectively. Specifically, the exergy balance equation for each component is shown in Table 5.

$$\dot{E}_{in,k} - \dot{E}_{out,k} - W_k - I_k = 0 \tag{29}$$

$$\theta_k = \frac{I_k}{\sum I} \tag{30}$$

where $\dot{E}_{in,k}$, $\dot{E}_{out,k}$, W_k, and I_k represent the exergy input, exergy output, external work, and exergy loss of the k^{th} component, respectively. θ is the exergy loss ratio of the component and $\Sigma\theta = 1$.

3.6. Performance evaluation

The net power generation of the system is shown as Eq. (31).

$$W_{net} = W_{SOFC} + W_{GT} + W_{CT} - W_{FP} - W_{CP} - W_{AC} \tag{31}$$

where W_{GT} consists of the composition of the power of GT1 and GT2, and W_{AC} consists of the power of AC1 and AC2.

The performance metrics of the system include net electrical efficiency and exergy efficiency, which are expressed as Eqs. (32) and (33), respectively.

$$\eta_{el} = \frac{W_{net}}{(\dot{m} \times LHV)_{fuel}} \tag{32}$$

$$\eta_{ex} = \frac{W_{net} + \dot{E}_{heating} + \dot{E}_{cooling}}{\dot{E}_{fuel,in}} = \frac{W_{net} + \dot{E}_{heating} + \dot{E}_{cooling}}{\dot{E}_{ch,F5} + \dot{E}_{ph,F1} - \dot{E}_{ph,F6}} \tag{33}$$

where LHV is the low heating value, 50 MJ/kg for CH_4.

3.7. Model verification

This section addresses model validation for the CLHG, SOFC, and TRCC sub-cycles within the proposed CCHP system. Table 6 juxtaposes our simulation results with those reported by Edrisi et al. [38] for the CLHG system, revealing a maximum deviation of 1.60 %. Fig. 2 shows the model validation for the SOFC based on literature [28], with voltage values deviating by a maximum of 2.65 % at a fuel utilization factor (Uti_{fuel}) of 0.9. Table 7 compares the temperatures at each node in the present TRCC system with those in Ref. [31,42]. The maximum temperature deviation of 0.42 % occurs at node 3. These findings confirm that the model errors for the three principal units of the CCHP system are within an acceptable margin, thereby underscoring the reliability of our simulation results.

4. Results and discussion

This section commences with an elucidation of the thermodynamic performance advantages of the proposed CCHP system. This is followed by an in-depth discussion of the energy and exergy performance of the system under the baseline design case. Finally, the impact of key design parameters on system performance is analyzed, and the maximum

Table 6
Validation results of CLHG system.

Reactors	Parameters		Ref. [38]	Simulation	Error (%)
Fuel reactor	Temperature (℃)		723	721.11	0.261
	Flow (kmol/s)		2.999	2.998	0.033
	Mole fraction (−)	CO_2	0.3333	0.3334	0.023
		H_2O	0.6665	0.6664	0.008
Stream reactor	Temperature (℃)		727	724.64	0.46
	Flow (kmol/s)		6.55	6.55	0
	Mole fraction (−)	H_2O	0.5938	0.5929	0.152
		H_2	0.4062	0.4071	0.222
Air reactor	Temperature (℃)		880	865.89	1.60
	Flow (kmol/s)		2.5380	2.5483	0.41

Table 5
Exergy balance equations for all components.

Components	$\dot{E}_{in}$	$\dot{E}_{out} + W_k$	I
FR&SR&AR	$\dot{E}_{F7}+\dot{E}_{W1}+\dot{E}_{A3}$	$\dot{E}_{F8}+\dot{E}_{A8}+\dot{E}_{W2}$	$\dot{E}_{F7}+\dot{E}_{W1}+\dot{E}_{A3}-(\dot{E}_{F8}+\dot{E}_{A8}+\dot{E}_{W2})$
GT1	$\dot{E}_{F8}-\dot{E}_{F9}$	$\dot{W}_{GT1}$	$\dot{E}_{F8}-\dot{E}_{F9}-\dot{W}_{GT1}$
HEX1	$\dot{E}_{F9}-\dot{E}_{F10}$	$\dot{E}_{A3}-\dot{E}_{A2}$	$\dot{E}_{F9}-\dot{E}_{F10}-(\dot{E}_{A3}-\dot{E}_{A2})$
HEX2	$\dot{E}_{F10}-\dot{E}_{F11}$	$\dot{E}_{F7}-\dot{E}_{F5}$	$\dot{E}_{F10}-\dot{E}_{F11}-(\dot{E}_{F7}-\dot{E}_{F5})$
HEX5	$\dot{E}_{F11}-\dot{E}_{F12}$	$\dot{E}_{4b}-\dot{E}_{3b}$	$\dot{E}_{F11}-\dot{E}_{F12}-(\dot{E}_{4b}-\dot{E}_{3b})$
Heater1	$\dot{E}_{F12}-\dot{E}_{F13}$	$\dot{E}_{9}-\dot{E}_{8}$	$\dot{E}_{F12}-\dot{E}_{F13}-(\dot{E}_{9}-\dot{E}_{8})$
GLS	$\dot{E}_{F13}$	$\dot{E}_{F14}+\dot{E}_{F15}$	$\dot{E}_{F13}-(\dot{E}_{F14}+\dot{E}_{F15})$
AC1	$\dot{W}_{AC1}$	$\dot{E}_{A2}-\dot{E}_{A1}$	$\dot{W}_{AC1}-(\dot{E}_{A2}-\dot{E}_{A1})$
AC2	$\dot{W}_{AC2}$	$\dot{E}_{A5}-\dot{E}_{A4}$	$\dot{W}_{AC2}-(\dot{E}_{A5}-\dot{E}_{A4})$
SOFC	$\dot{E}_{A6}+\dot{E}_{W2}$	$\dot{E}_{A7}+\dot{E}_{W1}+\dot{W}_{SOFC}$	$\dot{E}_{A6}+\dot{E}_{W2}-(\dot{E}_{A7}+\dot{E}_{W1}+\dot{W}_{SOFC})$
Mixer1	$\dot{E}_{A7}+\dot{E}_{A8}$	$\dot{E}_{A9}$	$\dot{E}_{A7}+\dot{E}_{A8}-\dot{E}_{A9}$
GT2	$\dot{E}_{A9}-\dot{E}_{A10}$	$\dot{W}_{GT2}$	$\dot{E}_{A9}-\dot{E}_{A10}-\dot{W}_{GT2}$
HEX3	$\dot{E}_{A10}-\dot{E}_{A11}$	$\dot{E}_{A6}-\dot{E}_{A5}$	$\dot{E}_{A10}-\dot{E}_{A11}-(\dot{E}_{A6}-\dot{E}_{A5})$
HEX4	$\dot{E}_{A11}-\dot{E}_{A12}$	$\dot{E}_{4a}-\dot{E}_{3a}$	$\dot{E}_{A11}-\dot{E}_{A12}-(\dot{E}_{4a}-\dot{E}_{3a})$
Heater2	$\dot{E}_{A12}-\dot{E}_{A13}$	$\dot{E}_{8}-\dot{E}_{7}$	$\dot{E}_{A12}-\dot{E}_{A13}-(\dot{E}_{8}-\dot{E}_{7})$
Mixer2	$\dot{E}_{4a}+\dot{E}_{4b}$	$\dot{E}_{4}$	$\dot{E}_{4a}+\dot{E}_{4b}-\dot{E}_{4}$
CT	$\dot{E}_{4}-\dot{E}_{5}$	$\dot{W}_{CT}$	$\dot{E}_{4}-\dot{E}_{5}-\dot{W}_{CT}$
CP	$\dot{W}_{CP}$	$\dot{E}_{2}-\dot{E}_{1}$	$\dot{W}_{CP}-(\dot{E}_{2}-\dot{E}_{1})$
REG	$\dot{E}_{5}-\dot{E}_{6}$	$\dot{E}_{3}-\dot{E}_{2}$	$\dot{E}_{5}-\dot{E}_{6}-(\dot{E}_{3}-\dot{E}_{2})$
FP	$\dot{W}_{FP}$	$\dot{E}_{F2}-\dot{E}_{F1}$	$\dot{W}_{FP}-(\dot{E}_{F2}-\dot{E}_{F1})$
Condenser1	$\dot{E}_{F2}-\dot{E}_{F3}$	$\dot{E}_{1}-\dot{E}_{6}$	$\dot{E}_{F2}-\dot{E}_{F3}-(\dot{E}_{1}-\dot{E}_{6})$
Condenser2	$\dot{E}_{F3}-\dot{E}_{F4}$	$\dot{E}_{F16}-\dot{E}_{F14}$	$\dot{E}_{F3}-\dot{E}_{F4}-(\dot{E}_{F16}-\dot{E}_{F14})$
Cooler	$\dot{E}_{F4}-\dot{E}_{F5}-\dot{E}_{F6}$	$\dot{E}_{11}-\dot{E}_{10}$	$\dot{E}_{F4}-\dot{E}_{F5}-\dot{E}_{F6}-(\dot{E}_{11}-\dot{E}_{10})$

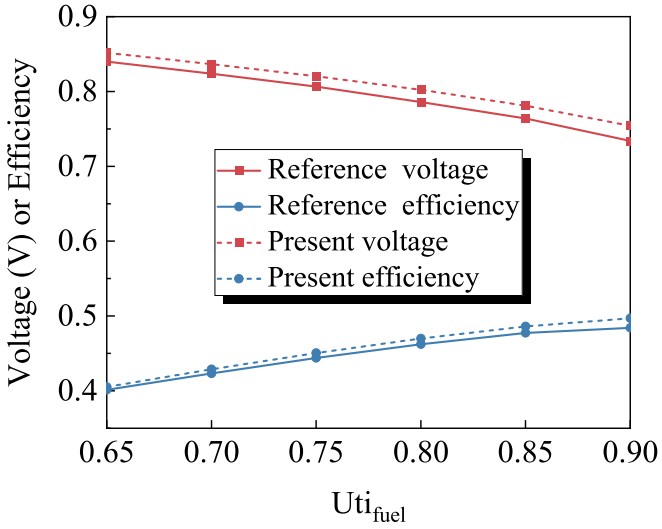

Fig. 2. Model validation results for SOFC [28].

Table 7
Validation results of TRCC system.

State points	Temperature (℃)		
	Ref. [42]	Ref. [31]	Present
1	15	15	15
2	22.974	22.993	22.998
3	30.548	30.42	30.41
4	95	95	95
5	36.188	36.148	36.146
6	24.263	24.309	24.312

output power in scenarios where the system is predominantly designed in the CHP or CCP mode is obtained.

4.1. Performance comparison

Table 8 compares the outcomes of the current system with those in Ref. [29] under the same input conditions. A notable observation is that the output power of the present system exceeds that of the reference system by 44.72 kW. This discrepancy can be attributed to two primary factors. One factor is the power-consuming carbon capture for the reference system while the zero-energy penalty carbon capture for the present system. Another reason is that the proposed system outputs cold energy through the LNG regasification unit, thereby allowing more waste heat to be supplied to the TRCC and heating units. Therefore, the electrical and exergy efficiencies of the proposed system are enhanced by 18.49 % and 13.16 %, respectively. However, the cooling power of the proposed system is 3.20 kW, significantly lower than that of the reference system of 57.14 kW. A feasible way to enhance cooling power is to increase the flow rate of LNG, but it can reduce the exergy efficiency of the system.

Table 8
Performance comparison of CCHP systems.

Item	Ref. [29]	Present
Input energy, kW	241.91	241.91
Input exergy, kW	249.37	266.47
Output power, kW	113.06	157.78
Heating power, kW	28.26	43.02
Cooling power, kW	57.14	3.20
Heating exergy, kW	1.78	2.65
Cooling exergy, kW	2.92	0.11
Electrical efficiency, %	46.74	65.23
Exergy efficiency, %	47.09	60.25

4.2. Thermodynamic analysis under baseline design case

Based on the design parameters outlined in Table 1, the thermodynamic performance and nodal physical properties of the system are delineated in Tables 9 and 10, respectively. The net power generation of the system is 149.41 kW, consisting of an output power of 3.00 kW from the CLHG unit, 130.69 kW from the SOFC-GT unit, and 15.72 kW from the TRCC unit. Since the total energy input to the CLHG unit amounts to 232.25 kW, the system achieves an electrical efficiency of 66.92 %. Additionally, the LNG regasification process contributes a cooling power of 11.40 kW and a cold exergy output of 0.40 kW. The heating unit delivers a power output of 36.06 kW and an exergy output of 2.22 kW. Since the total exergy input of the system is 279.40 kW, which is a sum of 232.36 kW chemical exergy and 47.03 kW physical exergy of the fuel, the exergy efficiency of the system is 53.94 %.

The detailed exergy flow distribution within the proposed system under the baseline design case is plotted in Fig. 3, which intuitively conveys the exergy input, output, and loss for each component. The exergy input to the system is mainly output in the form of electricity. Post-oxidation of CH_4 in the FR, the product gas progresses to GT1 with an exergy of 26.06 kW and generates electricity of 9.70 kW. The total exergy imported into the SOFC is 282.76 kW, of which 36.63 % is converted to electricity via chemical reactions. The two streams of nitrogen-rich air from the CLHG and SOFC units have an exergy of 122.22 kW, of which 50.33 % is converted to electricity by expansion in the GT2. The CO_2 enters the CT with an exergy of 39.23 kW and generates electricity of 17.19 kW through expansion. Furthermore, the large temperature difference between the two fluids leads to the highest exergy loss of 37.78 kW in condenser1, accounting for 29.50 % of the total exergy loss of the system. The irreversible chemical reactions destroy the exergy of the CLHG and SOFC units by 27.16 kW and 21.46 kW, respectively, ranking as the second- and third-highest exergy loss shares within the system. Other components exhibit relatively lower exergy losses. Regarding the individual contributions to exergy loss from each unit, as depicted in Fig. 4, the ranking from highest to lowest is as follows: the LNG regasification unit, the SOFC-GT unit, the CLHG unit, the TRCC unit, and the heating unit.

4.3. Parameter analysis

The results in Section 4.2 show that the output power of the SOFC-GT unit constitutes a substantial 86 % share of the overall system exergy output. This indicates that the parameters that can change the power of the SOFC-GT unit have a non-negligible impact on the system performance. Meanwhile, the variation of the exhaust gas parameters of the SOFC-GT driving the downstream units affects the overall system performance. Therefore, the flow rate of CH_4 and the fuel utilization, operating temperature, and operating pressure of the SOFC are considered pivotal design parameters. The analytical ranges of these

Table 9
Thermodynamic performance of the proposed system.

Item	Value
Input energy, kW	223.25
Input exergy, kW	279.40
CLHG unit output power, kW	3.00
SOFC-GT output power, kW	130.69
TRCC unit output power, kW	15.72
Heating power, kW	36.06
Cooling power, kW	11.40
Heating exergy, kW	2.22
Cooling exergy, kW	0.40
Electrical efficiency, %	66.92
Exergy efficiency, %	53.94

Table 10
Nodal thermodynamic properties of the system under the baseline design case.

Nodes	T/℃	p/MPa	$\dot{n}$/kmol·h^{-1}	h/kJ·kmol^{-1}	$\dot{E}$/kW	Composition (%)	
						CO_2	H_2O
1	−26.75	1.59	8.38	−409601	22.39	100	0
2	−20.15	13.30	8.38	−408999	23.46	100	0
3a	44.58	13.30	7.24	−402352	19.74	100	0
3b	44.58	13.30	1.14	−402352	3.10	100	0
3	44.58	13.30	8.38	−402352	22.84	100	0
4a	382.90	13.30	7.24	−378833	34.35	100	0
4b	324.79	13.30	1.14	−381861	4.90	100	0
4	375.02	13.30	8.38	−379244	39.23	100	0
5	199.18	1.59	8.38	−386630	19.20	100	0
6	45.65	1.59	8.38	−393277	15.51	0	100
7	25.00	0.10	43.08	−285811	0	0	100
8	34.93	0.10	43.08	−285063	0.146	0	100
9	65.00	0.10	43.08	−282797	2.22	0	100
10	25.00	0.10	27.18	−285811	0	0	100
11	5.00	0.10	27.18	−287321	0.401	0	100
F1	−162.00	0.10	13.01	−89434.5	3085.02	CH_4 (100 %)	
F2	−161.83	0.51	13.01	−89415.3	3085.05		
F3	−89.39	0.51	13.01	−78899.4	3040.39		
F4	−80.00	0.51	13.01	−78568.7	3039.70		
F5	10.00	0.51	1.00	−75412.9	233.47		
F6	10.00	0.51	12.01	−75412.9	2803.19		
F7	450.00	0.51	1.00	−54734.2	235.71		
F8	975.65	0.51	3.00	−254371	26.06	54.98	45.02
F9	728.22	0.10	3.00	−266014	15.61	54.98	45.02
F10	515.25	0.10	3.00	−275444	10.38	54.98	45.02
F11	349.79	0.10	3.00	−282337	7.07	54.98	45.02
F12	150.00	0.10	3.00	−290113	4.32	54.98	45.02
F13	45.00	0.10	3.00	−332587	0.065	54.98	45.02
F14	45.00	0.10	1.00	−392784	0.007	100	0
F15	45.00	0.10	2.00	−284305	0.027	0	100
F16	−78.46	0.10	1.00	−397048	0.261	100	0
						N_2	O_2
A1	25.00	0.10	3.88	−8.04	0	79.0	21.0
A2	234.50	0.51	3.88	6163.73	5.97	79.0	21.0
A3	470.00	0.51	3.88	13395.71	10.04	79.0	21.0
A4	25.00	0.10	20.06	−8.04	0	79.0	21.0
A5	234.50	0.51	20.06	6163.73	30.62	79.0	21.0
A6	500.00	0.51	20.06	14343.88	54.71	79.0	21.0
A7	910.00	0.51	18.73	27761.57	99.38	85.31	14.69
A8	1158.24	0.51	3.22	36074.39	22.84	97.64	2.36
A9	946.67	0.51	18.73	28980.64	122.07	87.09	12.91
A10	643.89	0.10	21.95	18890.21	53.48	87.09	12.91
A11	407.90	0.10	21.95	11412.65	25.01	87.09	12.91
A12	150.00	0.10	21.95	3653.22	3.68	87.09	12.91
A13	100.00	0.10	21.95	2184.92	1.44	87.09	12.91
						H_2O	H_2
W1	910.00	0.51	3.40	−179431	58.35	98.23	1.77
W2	1023.58	0.51	3.40	10158.77	228.05	43.13	56.87

parameters depend on existing studies [26–29]. Furthermore, all other parameters are held at their baseline design values when a parameter is analyzed.

4.3.1. *Flow rate of CH_4*

Alterations in the flow rate of CH_4 injected into the CLHG have a significant influence on H_2 production, thereby affecting the performance of the SOFC and its downstream units. Fig. 5 presents the impact of increasing fuel flow rate on system performance. When the fuel flow rate escalates from 1.0 kmol/h to 4 kmol/h, the electrical, exergy, and SOFC efficiencies of the system decrease from 66.92 %, 53.94 %, and 49.03 % to 60.83 %, 47.51 %, and 37.99 %, respectively. Fig. 6 illustrates the variation of SOFC performance and unit power with fuel flow rate to explain the degradation of system performance. As the fuel flow rate increases, the CLHG requires more water vapor to generate more H_2. Consequently, the H_2 supplementation and air intake are increased by 1.41 kmol/h and 86.33 kmol/h, respectively, to ensure that the SOFC can provide enough water vapor to the CLHG at a constant fuel utilization rate, as shown in Fig. 6(a). Synchronously, the current density of the SOFC increases by 446.23 mA/cm^2, but the voltage decreases by 0.17 V. Since the increase in current density dominates, the output power of the SOFC experiences an upswing. Nevertheless, the efficiency of the SOFC decreases to 37.99 % due to the augmented input of chemical energy from H_2. With the rise in exhaust gas flow rate, the heat recovery, heat dissipation, and flow rate of the working medium within the downstream units increase, resulting in enhanced power outputs for cooling, heating, and power, as shown in Fig. 6(b). Therefore, the reason for the decline in overall system performance is that the increase in fuel flow rate leads to more chemical energy being converted into heat and more energy being destroyed. Note that the increased flow rate of LNG augments the cooling power of the system while diminishing the exergy efficiency, as expected.

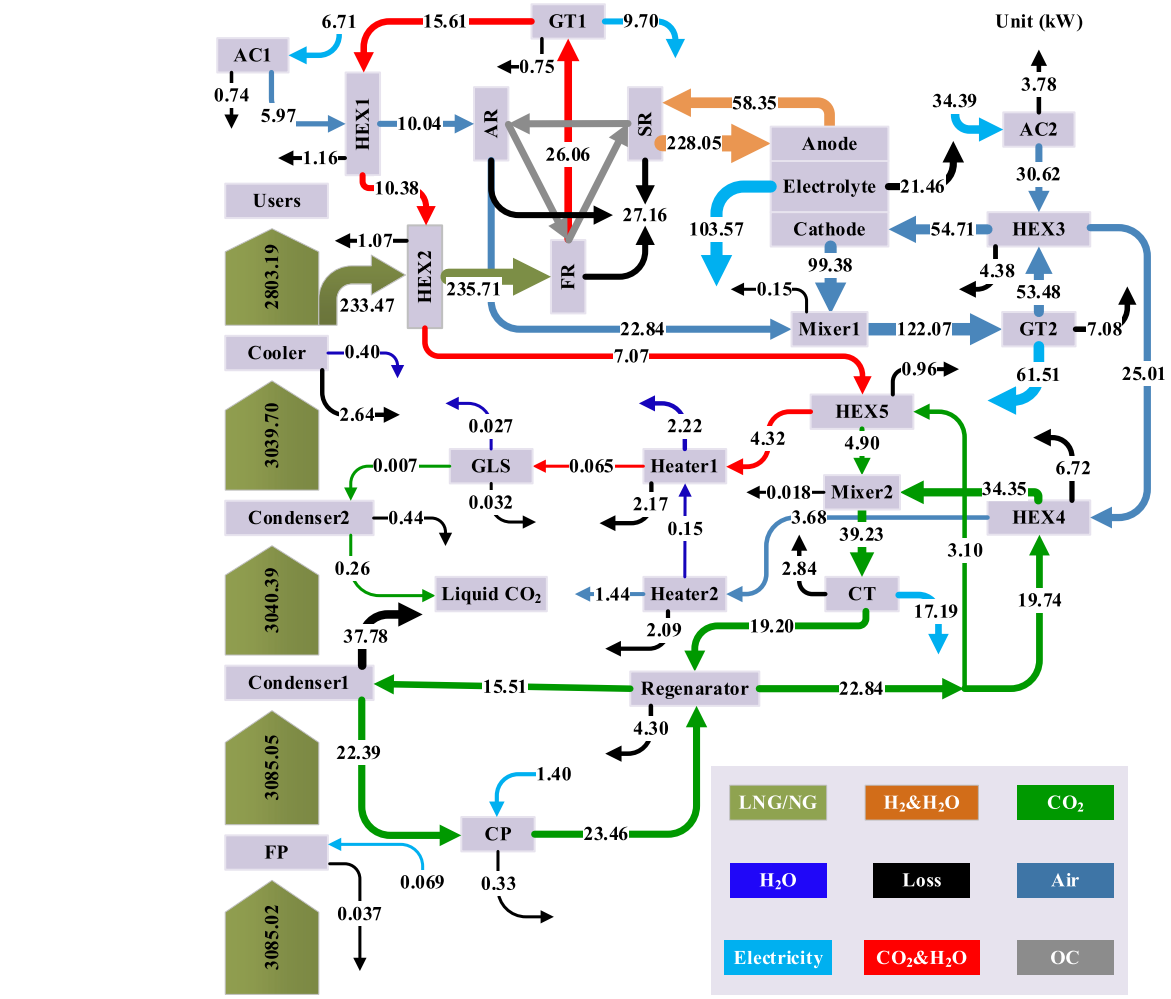

Fig. 3. Exergy flow diagram of the proposed system under design conditions.

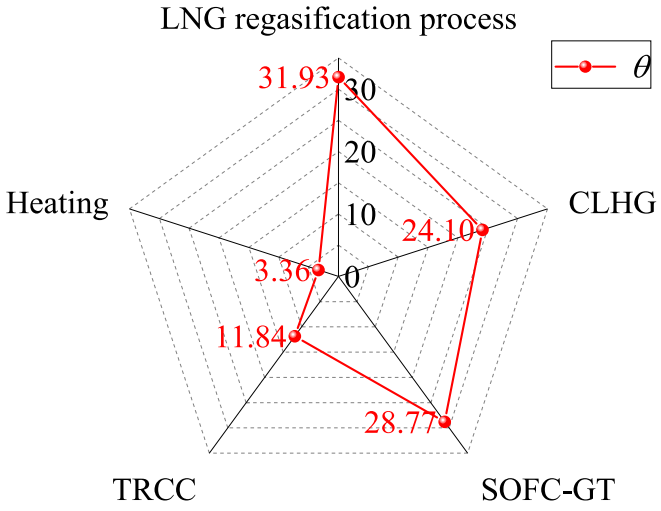

Fig. 4. Distribution of exergy losses for the units in the system.

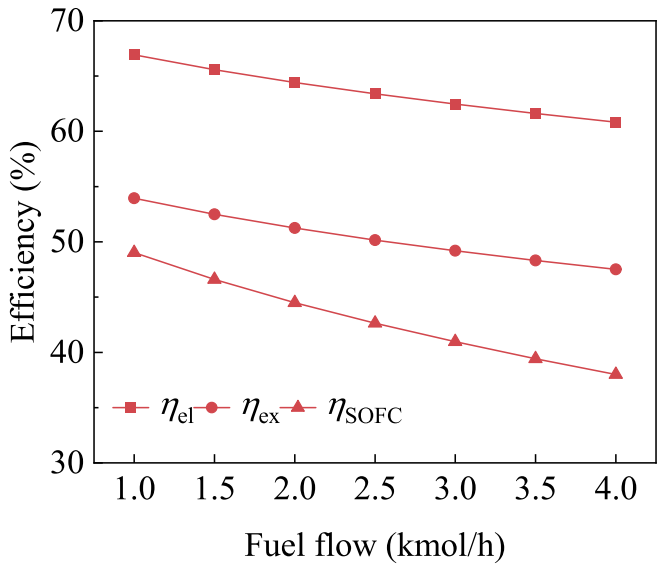

Fig. 5. Effect of fuel flow rate on system performance.

4.3.2. Fuel utilization of the SOFC

Fig. 7 shows the influence of fuel utilization on system performance. With the fuel utilization rate progressing from 0.65 to 0.95, the electrical and exergy efficiencies of the system decrease by 4.04 % and 4.47 %, respectively, while the SOFC efficiency first rises and then falls. The results in Fig. 8 can explain these phenomena.

Irrespective of the fuel utilization rate, the amount of H_2 consumed by the SOFC remains constant, aligning with the amount of H_2 produced

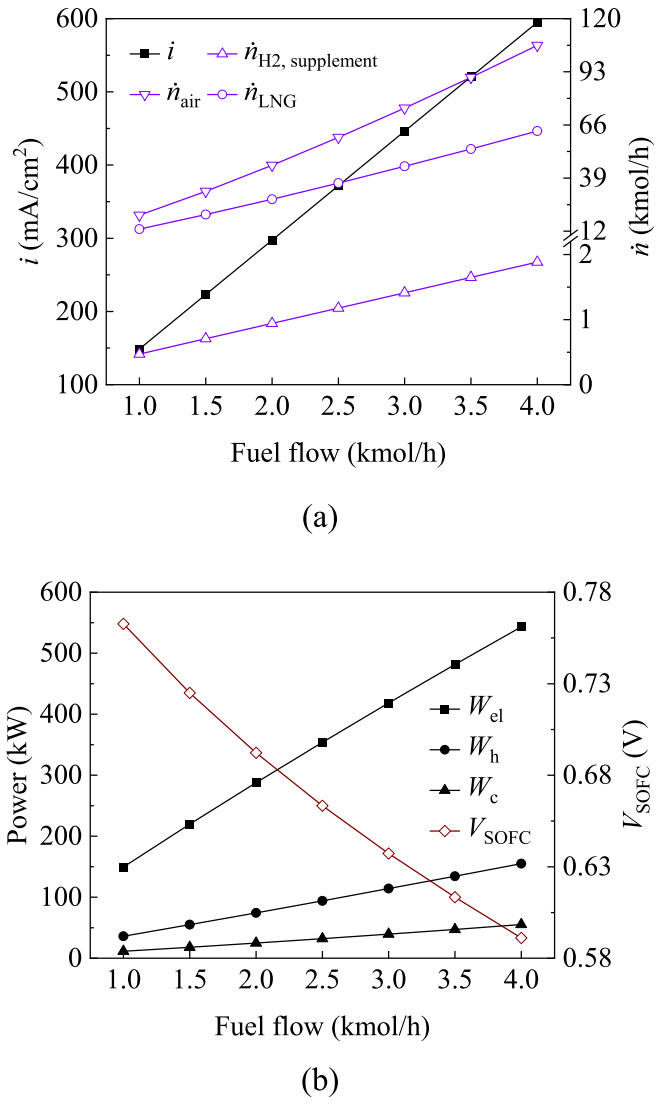

Fig. 6. Effect of fuel flow rate on system parameters (a) and power (b).

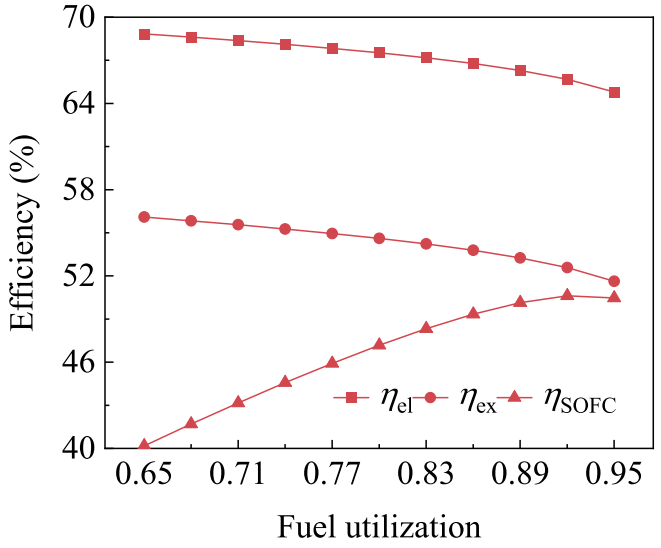

Fig. 7. Effect of fuel utilization on system performance.

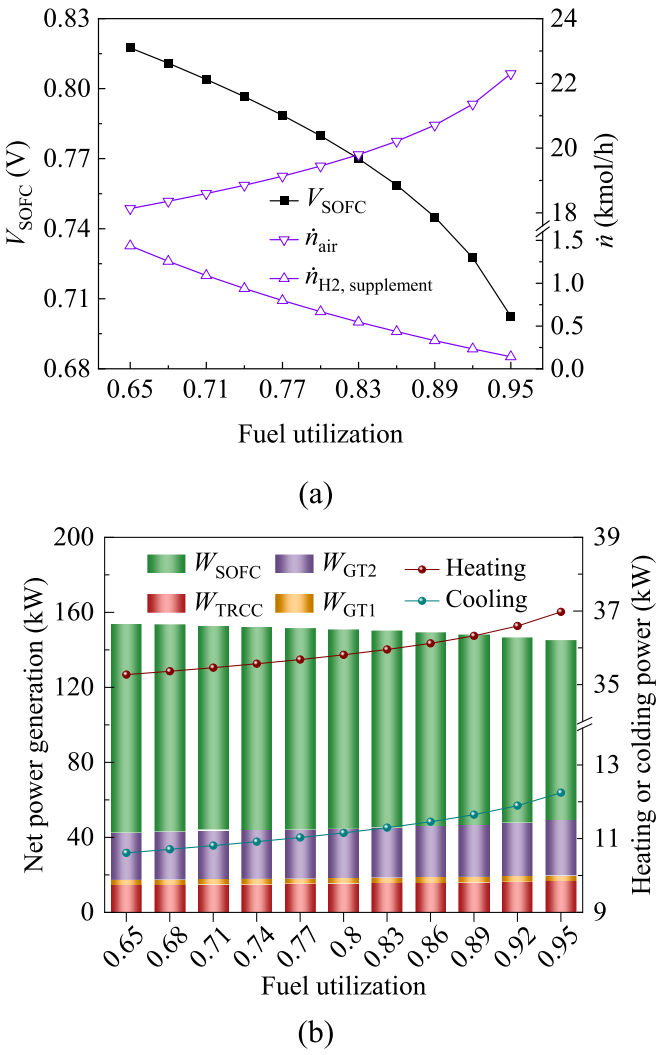

Fig. 8. Effect of fuel utilization on system parameters (a) and unit power (b).

by the CLHG. Consequently, an escalation in the fuel utilization rate leads to a reduction in H_2 supplementation to 0.14 kmol/h, as depicted in Fig. 8(a), which allows the SOFC to maintain a consistent current density of 148.74 mA/cm^2. Due to the discrepancy in H_2 quantity at the inlet and outlet of the SOFC anode, the increased fuel utilization induces a decrement in cell voltage by 0.115 V, consequently leading to a decrease in SOFC power by 15.62 kW, as illustrated in Fig. 8(b). Meanwhile, the chemical energy of H_2 entering the SOFC diminishes with escalating fuel utilization, resulting in a parabolic trend in SOFC efficiency. The decline in H_2 intake necessitates a corresponding increase in the air intake to uphold a consistent outlet temperature for the SOFC. The rising airflow increases the net power generation of the GT2 cycle and TRCC, in addition to enhancing the power for cooling and heating. Nonetheless, the resultant rise in downstream power generation is outstripped by the decline in SOFC power, culminating in an overall reduction in both the electrical and exergy efficiencies of the system. Furthermore, in practical applications of this system, any endeavor to enhance system performance by manipulating the fuel utilization rate entails a trade-off between the advantages stemming from improved performance and the disadvantages incurred due to H_2 supplementation.

4.3.3. *Operating temperature of the SOFC*

The operating temperature of the SOFC equals its outlet temperature, thereby influencing the system performance by acting on the CLHG and

the waste heat recovery units. The variation of system performance with operating temperature of SOFC is shown in Fig. 9. As the operating temperature rises from 800 °C to 1100 °C, the electrical efficiency of the system improves by 6.96 %, while the exergy efficiency and SOFC efficiency first increase and then decrease. The reasons behind these changes are presented in Fig. 10.

Fig. 10 (a) exemplifies that the voltage of the SOFC first increases and then decreases with rising operating temperature, making both the efficiency and output power of the SOFC change parabolically due to the constant current density. The rise in the outlet temperature of the SOFC to 1100 °C is achieved by reducing the amount of air intake to 12.95 kmol/h. This causes the net power generation of the GT2 cycle to drop by 6.01 kW despite an increasing turbine inlet temperature, as shown in Fig. 10(b). The heating power supplied by the system declines with the reduced airflow. However, the output power of the GT1 cycle and TRCC units improves by 0.91 kW and 7.09 kW, respectively, owing to the increase in their respective highest temperatures. Consequently, the net power generation of the system increases at a decreasing slope with the rising operating temperature of the SOFC. Additionally, the escalation in heat dissipation from the TRCC augments the flow rate of LNG by 1.47 kmol/h. This increases both the cooling power and the fuel physical exergy of the system, with the latter being chiefly responsible for the parabolic trend in the exergy efficiency. Therefore, a rise in the operating temperature of the SOFC causes a greater proportion of fuel chemical energy to be harnessed for electrical energy conversion while aggravating the exergy destruction of some components.

4.3.4. *Operating pressure of the upstream unit*

The operating pressure of the upstream unit plays a pivotal role in the overall performance of the system, as it significantly influences the power of the compression components, gas turbine, and SOFC. The variation of system performance with the operating pressure of the upstream unit is shown in Fig. 11. As the operating pressure escalates from 3 bar to 8 bar, the enhancements of 2.71 %, 4.63 %, and 2.57 % are observed in the electrical, exergy, and SOFC efficiencies of the system, respectively. And the rate of improvement in electrical and exergy efficiencies gradually diminishes. To elucidate the underlying mechanisms driving these performance variations, Fig. 12 presents the variation of the net output power of the units with operating pressure. Fig. 12(a) underscores that an increase in operating pressure augments the voltage to 0.78 V and reduces the amount of air intake to 19.35 koml/h for the SOFC. Since the constant amount of H_2 consumed leads to a constant current density, the power of the SOFC increases by 5.44

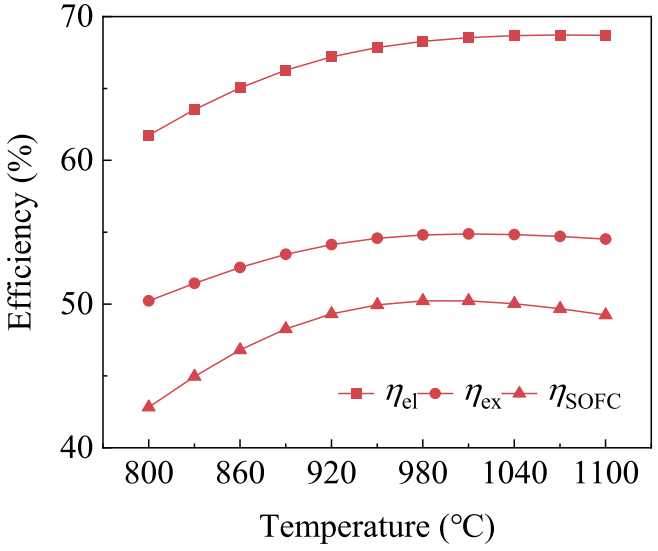

Fig. 9. Effect of operating temperature of SOFC on system performance.

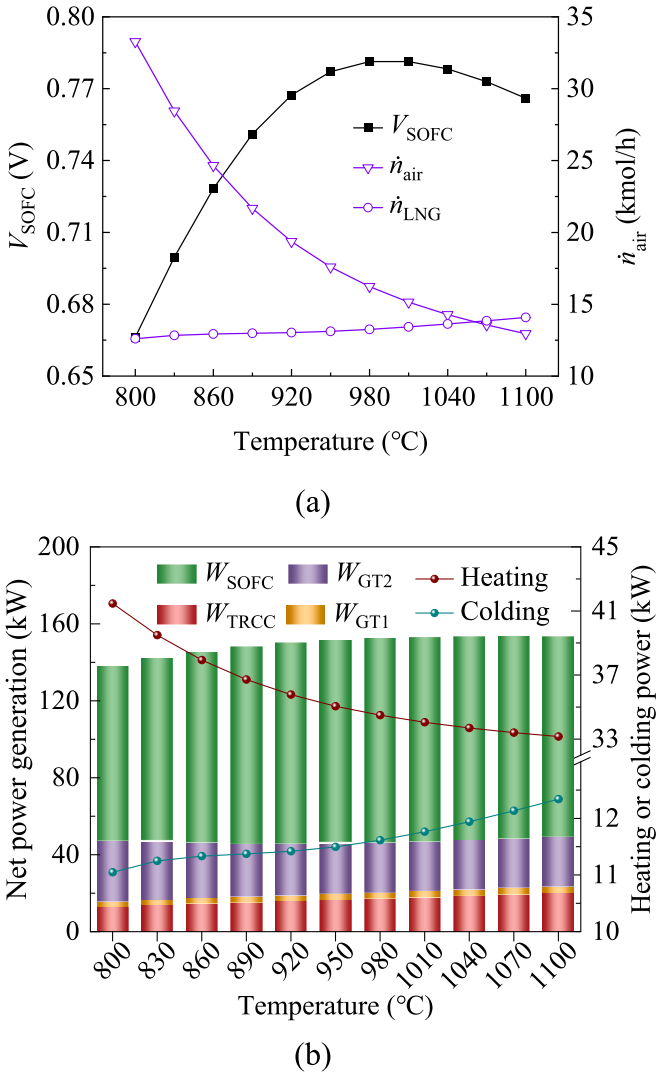

Fig. 10. Effect of operating temperature of SOFC on system parameters (a) and unit power (b).

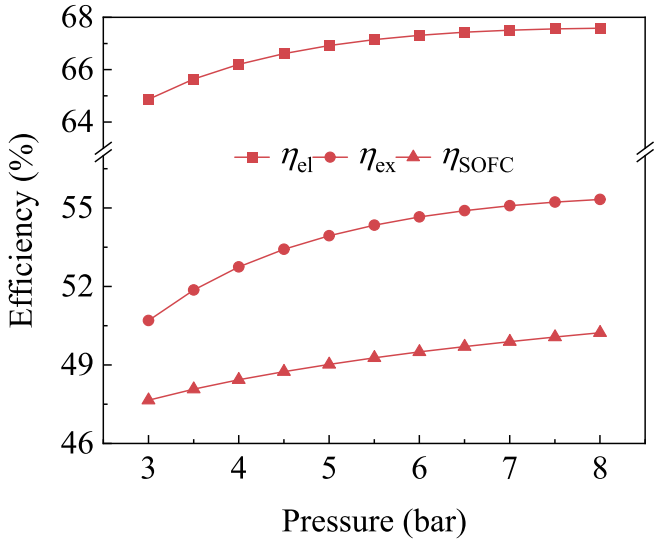

Fig. 11. Effect of operating pressure of upstream unit on system performance.

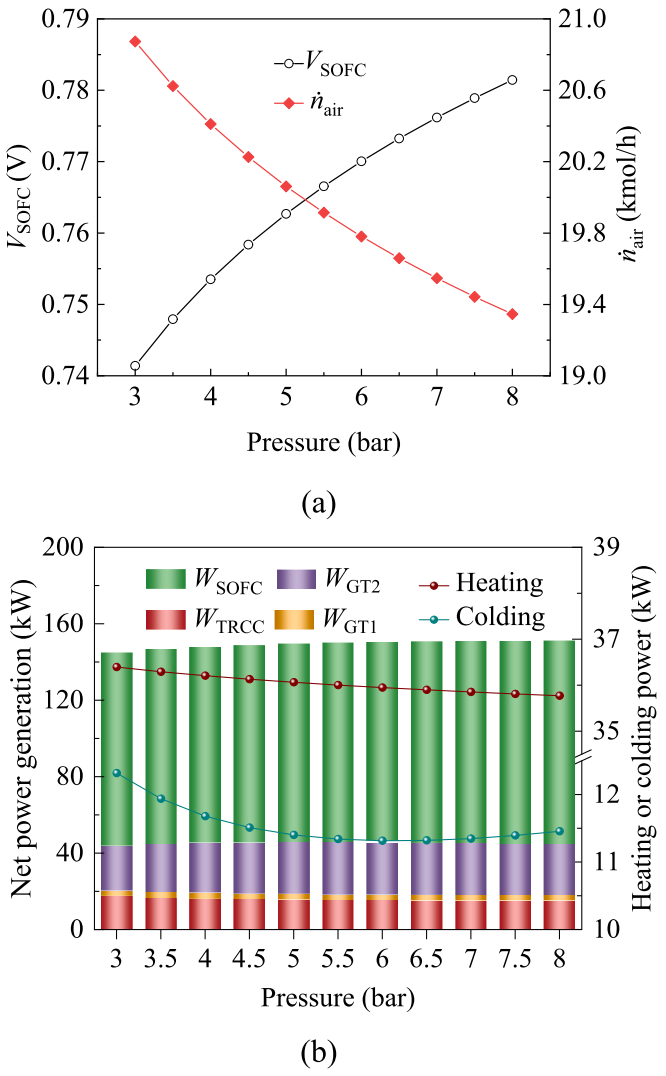

Fig. 12. Effect of operating pressure of upstream unit on system parameters (a) and unit power (b).

kW, as depicted in Fig. 12(b). In the GT1 and GT2 cycles, the heightened pressure causes their net power generation to first increase and then decrease. The elevation in expansion ratio declines the exhaust temperature of GT2, which, coupled with the reduced exhaust flow, attenuates the heat recovery within the downstream cycle. Consequently, the power outputs of the TRCC, heating, and cooling units exhibit varying degrees of reduction with the rising operating pressure of the upstream unit. Ultimately, the net power generation of the system ascends in a slope-decreasing manner, thus yielding a similar trend in both efficiencies.

4.3.5. *Bi-objective optimization considering cooling and heating modes*

Parametric analysis reveals that the cooling power or heating power of the system exhibits a contrasting trend to the net power generation under some design conditions. Therefore, it is necessary to implement a bi-objective optimization of the CHP- or CCP-dominated mode to the trade-off between the net power generation and the heating or cooling power of the system. A non-dominated sequential genetic algorithm (NSGA-II) is employed to complete the optimization, and the algorithm setup is consistent with Ref. [43].

The optimization outcomes for both dominant modes are illustrated in Fig. 13. The augmentation in cooling or heating power comes at the cost of a reduction in net power generation. Fig. 13(a) shows that as the cooling power of the system dominated by the CCP mode increases from 47.93 kW to 62.16 kW, its net power generation declines from 624.68 kW to 444.26 kW. Similarly, Fig. 13(b) exemplifies that an increase in heating power of the system dominated by the CHP mode from 131.66 kW to 193.40 kW results in a decrease in net power generation from 624.68 kW to 439.40 kW. The range of achievable net generation power is broader for the system dominated by the CHP model in comparison to the CCP model. Subsequently, the Pareto-optimal solution with the closest Euclidean distance to the ideal solution is obtained using the linear programming technique of multidimensional analysis of preference (LINMAP) [43]. The system performance corresponding to these two optimal solutions is detailed in Table 11. For scenarios necessitating more cooling capacity, the system design should select higher operating temperatures, lower operating pressures, and greater fuel utilization for the SOFC. Parameters exhibiting opposite trends are recommended to design the system for scenarios that require more heating power. An increase in the fuel flow rate injected into the CLHG unit offers a simultaneous enhancement in the cooling and heating capacity of the system. Consequently, the CCP-dominated system attains optimal electrical and exergy efficiencies of 62.98 % and 47.13 %, respectively, surpassing those achieved by the CHP-dominated one.

5. Conclusion

In this study, we introduce a novel CLHG/SOFC-driven CCHP system, which is fueled by the LNG regasification process. Upon confirming the thermodynamic advantages of this proposed configuration, we conduct an in-depth examination of the energy and exergy flow distributions within the system under the baseline design case. Subsequently, the influence of key design parameters on the system performance is thoroughly discussed. Finally, a bi-objective optimization of the cooling/

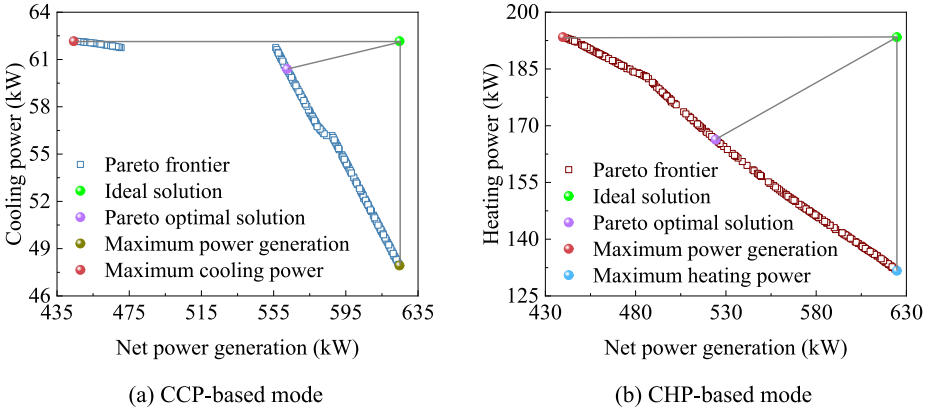

Fig. 13. Bi-objective optimization results for the system.

Table 11
Optimal system performance under both modes.

Mode	Optimal decision variables				System performance				
	Uti_{fuel} (−)	p_{CLHG} (bar)	T_{SOFC} (℃)	$\dot{n}_{CH4}$ (kmol/h)	η_{el} (%)	η_{ex} (%)	W_{el} (kW)	$W_{heating}$ (kW)	$W_{cooling}$ (kW)
CCP-based	0.93	3.0	1100.00	4	62.98	47.13	562.38	137.87	60.40
CHP-based	0.65	5.76	845.14	4	58.71	46.56	524.28	166.33	52.97

heating power and the net power generation of the system dominated by the CCP/CHP mode is carried out. The main findings are extracted as follows:

(1) Compared to the existing system, the proposed system reduces the layout's complexity and improves the overall performance by recovering LNG cold energy for cooling and direct liquefaction of excess CO_2. The proposed system has application potential for achieving near-zero carbon sustainable and efficient operation of fossil fuel-based combined cooling, heating, and power systems.

(2) Under the baseline design case, the system attains an electrical efficiency of 66.92 % and a thermal efficiency of 53.94 %. The power output of the SOFC-GT unit constitutes a substantial 86 % share of the overall system exergy output. The exergy loss ratio of 29.50 % for the condenser1 is the highest among the components. The constituent unit with the largest exergy loss contribution is the LNG regasification unit, followed by the SOFC-GT unit, the CLHG unit, the TRCC unit, and the heating unit. Therefore, a suitable cold storage medium is necessary to reduce the exergy loss in the condenser1 and LNG regasification unit.

(3) The increase in fuel flow augments the output power but reduces electrical and exergy efficiencies for the system. More hydrogen needs to be replenished when fuel utilization in the SOFC is used to improve system performance. The design of the CCP-dominated system is recommended to select higher operating temperatures, lower operating pressures, and greater fuel utilization for the SOFC. The parameters exhibiting opposite trends are recommended for designing the CHP-dominated system. These findings provide theoretical design guidance for the potential application of the proposed system in different regions. Ultimately, the optimal electrical and exergy efficiencies of the system predominantly designed in CCP mode surpass those in CHP mode by 4.27 % and 0.57 %, respectively.

While our study presents a more efficient CLHG/SOFC-driven CCHP system, it is essential to acknowledge that the source of the supplemented H_2 has not been explicitly addressed. Future studies are recommended to integrate the proposed system with advanced hydrogen production technologies, such as solar hydrogen production. Furthermore, efforts should be directed towards the off-design performance and control strategies of the system to cope with the peak-shaving demand of the load.

CRediT authorship contribution statement

Yadong Du: Writing – original draft, Validation, Software, Methodology, Investigation, Data curation. **Zhiyi Yu:** Writing – review & editing, Visualization, Methodology, Funding acquisition. **Ce Yang:** Writing – review & editing, Supervision, Resources, Project administration, Funding acquisition, Conceptualization. **Haimei Wang:** Writing – review & editing, Validation, Data curation. **Buchen Wu:** Writing – review & editing, Visualization, Resources, Formal analysis.

Declaration of competing interest

The authors declare that they have no known competing financial interests or personal relationships that could have appeared to influence the work reported in this paper.

Data availability

Data will be made available on request.

Acknowledgements

This study is supported by the Beijing Municipal Natural Science Foundation (Grant No. 3212021). Further, one of the authors, Yadong Du, gratefully acknowledges the support of the China Scholarship Council in providing him the financial support to facilitate his research exchange program at the National University of Singapore.

References

[1] Hydrogen Council, Path to hydrogen competitiveness: a cost perspective, Belgium, 2020.
[2] M.S. Alam, T.A. Chowdhury, A. Dhar, et al., Solar and wind energy integrated system frequency control: A critical review on recent developments, Energies 16 (2) (2023) 812.
[3] Y. Du, Z. Yu, W. Sun, et al., Chemical looping combustion-driven cooling and power cogeneration system with LNG cold energy utilization: Exergoeconomic analysis and three-objective optimization, Energy 295 (2024) 130877.
[4] G. Lozza, P. Chiesa, Natural gas decarbonization to reduce CO2 emission from combined cycles—Part I: Partial oxidation, J. Eng. Gas Turbines Power 124 (1) (2002) 82–88.
[5] K.A. Baumert, O. Blanchard, S. Llosa, et al., Options for Protecting the Climate, World Resources Institute, Washington, DC, 2002.
[6] Y. Du, Z. Yu, C. Yang, et al., Techno-economic optimization of the combined supercritical carbon dioxide and air Brayton cycles driven by copper-based chemical looping combustion, Energy Fuel 38 (3) (2024) 2305–2318.
[7] H.J. Richter, K.F. Knoche, Reversibility of combustion processes, Efficiency and Costing: American Chemical Society, 1983, pp. 71-85.
[8] I. Adanez-Rubio, M. Arjmand, H. Leion, P. Gayan, A. Abad, T. Mattisson, A. Lyngfelt, Investigation of combined supports for Cu-based oxygen carriers for chemical-looping with oxygen uncoupling (CLOU), Energy Fuel 27 (7) (2013) 3918–3927.
[9] K.S. Kang, C.H. Kim, K.K. Bae, et al., Oxygen-carrier selection and thermal analysis of the chemical-looping process for hydrogen production, Int. J. Hydrogen Energy 35 (22) (2010) 12246–12254.
[10] Q. Hao, L. Zhu, J. Fan, et al., Zero-energy penalty carbon capture and utilization system based on CLHG integrating SOFC for power and methanol cogeneration, Energ. Conver. Manage. 295 (2023) 117658.
[11] Y. De Vos, M. Jacobs, I. Van Driessche, et al., Processing and characterization of Fe-based oxygen carriers for chemical looping for hydrogen production, Int. J. Greenhouse Gas Control 70 (2018) 12–21.
[12] M. Rydén, M. Arjmand, Continuous hydrogen production via the steam–iron reaction by chemical looping in a circulating fluidized-bed reactor, Int. J. Hydrogen Energy 37 (6) (2012) 4843–4854.
[13] F. Kong, C. Li, Y. Zhang, et al., Hydrogen production from natural gas using an iron-based chemical looping technology: process modeling, heat integration, and exergy analysis, Energ. Technol. 8 (8) (2020) 1900377.
[14] X. Yan, H. Liu, M. Luo, et al., Performance of hydrogen and power co-generation system based on chemical looping hydrogen generation of coal, Int. J. Hydrogen Energy 48 (30) (2023) 11180–11190.
[15] Y. He, L. Zhu, L. Li, et al., Zero-energy penalty carbon capture and utilization for liquid fuel and power cogeneration with chemical looping combustion, J. Clean. Prod. 235 (2019) 34–43.
[16] M. Ghannadi, I. Dincer, Evaluation of iron-based chemical looping for hydrogen production from biomass using combined power cycle with carbon capturing and storage, Sustainable Energy Technol. Assess. 59 (2023) 103418.
[17] B. Ghorbani, S. Zendehboudi, N.M.C. Saady, et al., Hydrogen storage in North America: Status, prospects, and challenges, J. Environ. Chem. Eng. 11 (3) (2023) 109957.
[18] B. Ghorbani, S. Zendehboudi, Y. Zhang, et al., Thermochemical water-splitting structures for hydrogen production: Thermodynamic, economic, and environmental impacts, Energ. Conver. Manage. 297 (2023) 117599.
[19] B. Ghorbani, S. Zendehboudi, N.M.C. Saady, et al., Strategies to improve the performance of hydrogen storage systems by liquefaction methods: a comprehensive review, ACS Omega 8 (21) (2023) 18358–18399.

[20] N. Chitgar, M.A. Emadi, A. Chitsaz, et al., Investigation of a novel multigeneration system driven by a SOFC for electricity and fresh water production, Energ. Conver. Manage. 196 (2019) 296–310.
[21] T. Ni, J. Si, X. Gong, et al., Thermodynamic and economic analysis of a novel cascade waste heat recovery system for solid oxide fuel cell, Energ. Conver. Manage. 259 (2022) 115562.
[22] C. Zhang, L. Zhu, Q. Hao, et al., Thermodynamic and exergoeconomic evaluation of coal and biomass co-gasification as solid oxide fuel cell feed coupled with supercritical carbon dioxide and organic Rankine cycle, Energ. Conver. Manage. 300 (2024) 117951.
[23] Y. Liu, J. Han, H. You, Exergoeconomic analysis and multi-objective optimization of a CCHP system based on SOFC/GT and transcritical CO2 power/refrigeration cycles, Appl. Therm. Eng. 230 (2023) 120686.
[24] R. Zeng, J. Gan, B. Guo, et al., Thermodynamic performance analysis of solid oxide fuel cell-combined cooling, heating and power system with integrated supercritical CO2 power cycle-organic Rankine cycle and absorption refrigeration cycle, Energy 283 (2023) 129133.
[25] M.U. Azhar, M. Anwar, U.M. Khan, et al., Thermodynamic analysis of different modes of a multigeneration SOFC-CCHP system with freshwater production and LNG cold energy utilization, Energ. Conver. Manage. 297 (2023) 117730.
[26] H. Zhao, Z. Zhao, H. Wang, Thermodynamic performance study of the CLHG/SOFC combined cycle system with CO2 recovery, Energ. Conver. Manage. 223 (2020) 113319.
[27] H. Wang, H. Zhao, H. Du, et al., Thermodynamic performance study of a new diesel-fueled CLHG/SOFC/STIG cogeneration system with CO2 recovery, Energy 246 (2022) 123326.
[28] H. Wang, H. Zhao, Z. Zhao, Thermodynamic performance study of a new SOFC–CCHP system with diesel reforming by CLHG to produce hydrogen as fuel, Int. J. Hydrogen Energy 46 (44) (2021) 22956–22973.
[29] Z. Ma, J. Wang, F. Dong, et al., Thermodynamic analysis of fuel-cell-based combined cooling, heating, and power system integrated solar energy and chemical looping hydrogen generation, Energy 238 (2022) 121974.
[30] S.H. Cha, S.I. Na, Y.H. Lee, et al., Thermodynamic analysis of a gas turbine inlet air cooling and recovering system in gas turbine and CO2 combined cycle using cold energy from LNG terminal, Energ. Conver. Manage. 230 (2021) 113802.
[31] R. Su, Z. Yu, L. Xia, et al., Performance analysis and multi-objective optimization of an integrated gas turbine/supercritical CO2 recompression/transcritial CO2 cogeneration system using liquefied natural gas cold energy, Energ. Conver. Manage. 220 (2020) 113136.
[32] B. Li, S. Wang, Thermo-economic analysis and optimization of a cascade transcritical carbon dioxide cycle driven by the waste heat of gas turbine and cold energy of liquefied natural gas, Appl. Therm. Eng. 214 (2022) 118861.
[33] W. Liang, Z. Yu, S. Bai, et al., Study on a near-zero emission SOFC-based multi-generation system combined with organic Rankine cycle and transcritical CO2 cycle for LNG cold energy recovery, Energ. Conver. Manage. 253 (2022) 115188.
[34] Y. Liu, J. Han, H. You, Performance analysis of a CCHP system based on SOFC/GT/CO2 cycle and ORC with LNG cold energy utilization, Int. J. Hydrogen Energy 44 (56) (2019) 29700–29710.
[35] W.Y. Yang, W. Cao, J. Kim, et al., Applied Numerical Methods Using MATLAB, John Wiley & Sons, 2020.
[36] K.I.M. Al-Malah, Aspen Plus: Chemical Engineering Applications, John Wiley & Sons, 2022.
[37] E.W. Lemmon, M.L. Huber, M.O. McLinden, NIST reference fluid thermodynamic and transport properties–REFPROP, NIST Standard Reference Database 2002 (23) (2002) v7.
[38] A. Edrisi, Z. Mansoori, B. Dabir, et al., Hydrogen, nitrogen and carbon dioxide production through chemical looping using iron-based oxygen carrier–A Green plant for H2 and N2 production, Int. J. Hydrogen Energy 39 (20) (2014) 10380–10391.
[39] W. Zhang, E. Croiset, P.L. Douglas, et al., Simulation of a tubular solid oxide fuel cell stack using AspenPlusTM unit operation models, Energ. Conver. Manage. 46 (2) (2005) 181–196.
[40] Y. Haseli, I. Dincer, G.F. Naterer, Thermodynamic analysis of a combined gas turbine power system with a solid oxide fuel cell through exergy, Thermochim Acta 480 (1–2) (2008) 1–9.
[41] T.J. Kotas, The Exergy Method of Thermal Plant Analysis, Paragon Publishing, 2012.
[42] E. Cayer, N. Galanis, M. Desilets, et al., Analysis of a carbon dioxide transcritical power cycle using a low temperature source, Appl. Energy 86 (7–8) (2009) 1055–1063.
[43] Y. Du, L. Wang, Z. Yu, et al., Multi-objective optimization of thermoeconomic and component size of supercritical carbon dioxide recompression cycle based on small-scale lead-cooled fast reactor, Int. J. Energy Res. 46 (10) (2022) 13570–13589.